JOURNAL OF APPLIED CRYSTALLOGRAPHY

ISSN 1600-5767

Spin echo modulated small-angle neutron scattering using superconducting magnetic Wollaston prisms

Fankang Li,[a]* Steven R. Parnell,[b] Hongyu Bai,[c] Wencao Yang,[a] William A. Hamilton,[d] Brian B. Maranville,[e] Rana Ashkar,[d,e,f] David V. Baxter,[a] J. Ted Cremer[g] and Roger Pynn[a,d]*

[a]Center for the Exploration of Energy and Matter, Indiana University, 2401 Milo B Sampson Lane, Bloomington, IN 47408, USA, [b]Faculty of Applied Sciences, Delft University of Technology, Mekelweg 15, Delft, 2629 JB, The Netherlands, [c]National High Magnetic Field Laboratory, Tallahassee, FL 32310, USA, [d]Neutron Sciences Directorate, Oak Ridge National Laboratory, PO Box 2008, Oak Ridge, TN 37830, USA, [e]National Institute of Standards and Technology, Gaithersburg, MD 20899, USA, [f]Materials Science and Engineering Department, University of Maryland, College Park, MD 20742, USA, and [g]Adelphi Technology Inc., Redwood City, CA 94063, USA. *Correspondence e-mail: fankli@indiana.edu, pynn@mrl.ucsb.edu

Received 17 June 2015
Accepted 13 November 2015

Edited by D. I. Svergun, European Molecular Biology Laboratory, Hamburg, Germany

Keywords: magnetic Wollaston prisms; Larmor labeling; spin echo modulated small-angle neutron scattering (SEMSANS); neutron spin echo; correlation functions.

The spin echo modulated small-angle neutron scattering technique has been implemented using two superconducting magnetic Wollaston prisms at a reactor neutron source. The density autocorrelation function measured for a test sample of colloidal silica in a suspension agrees with that obtained previously by other neutron scattering methods on an identically prepared sample. The reported apparatus has a number of advantages over competing technologies: it should allow larger length scales (up to several micrometres) to be probed; it has very small parasitic neutron scattering and attenuation; the magnetic fields within the device are highly uniform; and the neutron spin transport across the device boundaries is very efficient. To understand quantitatively the results of the reported experiment and to guide future instrument development, Monte Carlo simulations are presented, in which the evolution of the neutron polarization through the apparatus is based on magnetic field integrals obtained from finite-element simulations of the various magnetic components. The Monte Carlo simulations indicate that the polarization losses observed in the experiments are a result of instrumental artifacts that can be easily corrected in future experiments.

1. Introduction

Small-angle neutron scattering (SANS) is a powerful technique to study the structures of materials of interest in chemistry, biology and engineering on length scales of 10–100 nm (Feigin & Svergun, 1987). Because the neutron wavelengths used for SANS are typically ∼0.5 nm, the scattering angle, given by Bragg's law, is of the order of one degree. Measuring such an angle accurately requires the incident neutron beam to be highly collimated, which limits the intensity of scattered neutrons. To measure length scales beyond 100 nm, ultra-small-angle neutron scattering (USANS) (Schaefer & Agamalian, 2004; Bonse & Hart, 1965) can be used. USANS is performed using aligned perfect single crystals to introduce a precise correlation between neutron trajectory and neutron wavelength. A second identical single crystal is used to analyze the scattered beam. However, in this case too, the required collimation and wavelength definition reduces the usable neutron flux significantly.

Instead of directly measuring the neutron scattering angles, several alternative approaches encode the scattering angle using the Larmor precession of the neutron polarization through a series of well defined magnetic fields (Krouglov *et*

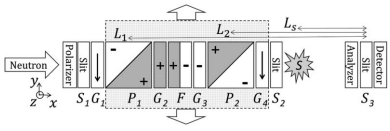

al., 2003; Bouwman *et al.*, 1999; Parnell *et al.*, 2015; Strobl, Tremsin *et al.*, 2012; Strobl, Weider *et al.*, 2012). These Larmor methods include spin echo small-angle neutron scattering (Bouwman *et al.*, 1999; Pynn *et al.*, 2008; Rekveldt, 1996; Bouwman *et al.*, 2000; Major *et al.*, 2009) (SESANS) and spin echo modulated small-angle neutron scattering (Bouwman *et al.*, 1999; Strobl, Tremsin *et al.*, 2012; Strobl, Weider *et al.*, 2012; Gähler, 2006) (SEMSANS). Even though these two methods are both implemented using Larmor encoding and both measure the same correlation function for the sample, they differ in concept. As shown in Fig. 1(*a*), a SESANS instrument can be constructed using four identical magnetic Wollaston prisms (Pynn *et al.*, 2009; Li *et al.*, 2014) (WPs), each with an inclined interface separating oppositely directed, triangular-shaped magnetic field regions. Like their optic counterparts, these WPs spatially separate the two different neutron spin states so that, in a SESANS measurement, these states interact with the sample at different points, separated by a distance called the spin echo length (denoted by ξ). The interference of the two states, mediated by the second pair of WPs, yields a neutron polarization that is related to the scattering-length-density autocorrelation function of the sample [equation (1)], measured at a distance equal to the spin echo length, provided the spin echo condition is satisfied. This condition ensures that, to leading order, the total Larmor phase is zero, independent of the neutron divergence angle, at the point in space where the neutron polarization is measured.

SEMSANS is more usefully described in terms of classical Talbot interferometry using light (Brezger *et al.*, 2002; Gähler, 2006). SEMSANS can be implemented using only two WPs with the two neutron spin states taking the paths shown in Fig. 1(*b*). These paths can be deduced simply from an application of Snell's law, taking into account the fact that the two

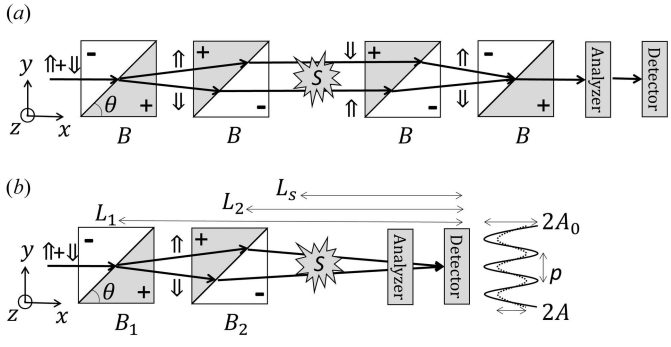

Figure 1
Schematics of the SESANS (*a*) and SEMSANS (*b*) setups using magnetic WPs, with the average wavevectors of the two neutron spin states denoted by arrows. The constant magnetic field in which the WPs are embedded is along the **y** direction and the incident neutrons are polarized in this direction. Fields inside the WPs are along either **z** or $-$**z**, as indicated in the figures. The symbols $\Uparrow$ and $\Downarrow$ indicate eigenstates of the S_z spin operator. At an interface of magnetic field reversal, each of the two spin states will be flipped. For SEMSANS, the final magnetic field boundary of the second WP acts as a $\pi/2$ spin flipper, after which only the projection of the polarization vector along the **y** direction can be preserved. For SEMSANS, the spatial oscillation of the measured intensity on the detector with (A) and without (A_0) sample is denoted as dashed and solid curves, respectively, and p is the spatial oscillation period.

neutron spin states have slightly different wavevectors in the magnetic fields generated by the WPs. Because the magnetic fields in the WPs are chosen so that $B_1L_1 = B_2L_2$ the two states converge and meet at the position of the neutron detector shown in the figure. As shown in the following section, this condition on B_1 and B_2 ensures that each neutron's contribution to the intensity at any point on the detector depends only on its y coordinate at the detector [see coordinate axes in Fig. 1(*b*)] and is independent of the angle a neutron trajectory makes with the optic axis of the apparatus (Gähler, 2006). Note the similarity of this condition to that used to define the spin echo position for SESANS: in both cases we demand a result that is independent of the neutron divergence angle. In our setup, only the y component of the neutron polarization is preserved after the neutrons leave the second WP. This polarization can be analyzed anywhere after the second WP with the same result. Whatever the position of the polarization analyzer, the measured polarization varies sinusoidally across the detector (in the **y** direction) with a period of p because each WP introduces a (different) Larmor phase between the neutron spin states that depends linearly on the y coordinate and the analyzed polarization is proportional to the cosine of this phase.

The sinusoidal modulation of the beam intensity at the detector is indicated in Fig. 1(*b*). It is important to note that any technology that produces an intensity modulation at the detector could be used to measure scattering, as was shown for Talbot interferometry with light many years ago (Brezger *et al.*, 2002). Scattering from the sample reduces the visibility (normalized amplitude) of the intensity modulation. For example, modulated intensity produced by diffraction gratings has been used with incoherent sources of both neutrons and X-rays by Pfeiffer *et al.* (2006) to measure the scattering produced by spatial variations of the refractive index of a sample. In SEMSANS, the ratio of the visibilities of the intensity modulation, measured with and without a sample, gives exactly the same projection of the sample density autocorrelation function as is obtained by SESANS (Andersson *et al.*, 2008; Strobl, 2014). Provided the detector is placed where the two spin states meet [*i.e.* the detector position in Fig. 1(*b*)], the spin echo length for which correlations are measured with SEMSANS is equal to the spatial separation of the two neutron spin states at the sample, just as it is for SESANS. A practical consequence of this is that, for WPs with a given maximum magnetic field, the spin echo length achievable on a beamline equipped with SEMSANS will be less than for SESANS because the second WP has the highest field while the first sets the maximum spin echo length obtainable. Nevertheless, both methods can measure the correlation function of the sample at longer length scales than SANS and the methods can be used, in principle, with poorly collimated neutron beams, greatly increasing the usable neutron flux.

Although the detailed expressions for the quantities measured by both SESANS and SEMSANS have been given by other authors (Bouwman *et al.*, 2011; Strobl, Tremsin *et al.*, 2012; Strobl, Weider *et al.*, 2012; Rekveldt, 1996; Strobl, 2014),

it is worth exploring why both of these techniques measure the same correlation function. For SESANS, the Larmor phase difference between the two spin states generated by the WPs before the sample is cancelled by the WPs after the sample provided there is no scattering. This cancellation results in a spin echo. If scattering occurs, the Larmor phase difference between the states changes by an amount equal to $\mathbf{Q} \cdot \boldsymbol{\xi}$, where $\mathbf{Q}$ is the scattering vector and $\boldsymbol{\xi}$ is the spin echo length (Rekveldt, 1996). This result is easily proved using Snell's law for the neutron states passing through the WPs. Because the polarization analyzer measures a polarization equal to the cosine of the Larmor phase, the contribution of the scattering to the measured polarization is simply the neutron scattering cross section times $\cos(\mathbf{Q} \cdot \boldsymbol{\xi})$, integrated over all values of $\mathbf{Q}$, *i.e.* the Fourier transform of the scattering. Adding in the contribution to the polarization from the unscattered neutrons and accounting for multiple scattering (Rekveldt *et al.*, 2002) yields the well known result for the normalized spin echo polarization P/P_0 measured in SESANS:

$$P/P_0 = \exp\{\Sigma_t[G(\xi) - 1]\}. \quad (1)$$

In this equation, Σ_t is the total probability for single scattering in any direction by the sample and $G(\xi)$ is a projection of the scattering-length-density autocorrelation function (Andersson *et al.*, 2008).

For SEMSANS, the phases generated by the two WPs are not balanced, so the Larmor phase varies linearly with y after the second WP, resulting in a modulated neutron intensity after the polarization analyzer. The normalized intensity of this modulation (*i.e.* the intensity at any point, measured with respect to the mean intensity and normalized to the amplitude of the modulation) is described by a cosine function. In the absence of background, the contribution of scattered neutrons to the intensity at any point, y, on the detector is simply equal to the probability that the sample scatters through an angle $2\theta_s$ times the intensity of the beam incident on the sample at the point $(y - L_s\, 2\theta_s)$, where the distance L_s, defined in Fig. 1(*b*), is the distance between the sample and the detector. Because of the beam modulation, the normalized intensity of the incident beam at this point is just $\cos[2\pi(y - L_s\, 2\theta_s)/p]$. Substituting for $2\theta_s$ (*i.e.* $2\theta_s = \lambda Q/2\pi$) and integrating over Q gives the total scattering contribution to the measured normalized intensity at position y. This expression is the same Fourier transform that is found for SESANS with the argument of the cosine equal to $Q\lambda L_s/p$. Thus, by analogy with the definition of the spin echo length for SESANS, the length probed by SEMSANS is $\lambda L_s/p$. Adding in the unscattered beam and dividing by the normalized intensity of the modulation without the sample follows exactly the same recipe as for SESANS so the end result has the same functional form as for SESANS, namely that given in equation (1). Notice, however, that this result applies for each y value on the detector for SEMSANS rather than resulting from an integral over the whole detector as for SESANS.

The relation between SEMSANS and SESANS is reminiscent of that between MIEZE (modulation of intensity by zero effort) (Gähler *et al.*, 1992) and NRSE (Golub & Gähler, 1987) (neutron resonant spin echo). For both SEMSANS and MIEZE, all spin manipulations are performed before the sample, allowing the sample to be placed in an environment, such as a high magnetic field, that could not be used with the precessing neutron polarization employed by NRSE and SESANS. However, just as MIEZE requires a neutron detector with a good time resolution while NRSE does not, SEMSANS needs a neutron detection method with good spatial resolution to measure the intensity fringes, while SESANS only needs an integrating detector. These methods are thus complementary in a way similar to Talbot and Lau interferometry.

In the SEMSANS experiment described in this paper, we used two high-temperature superconducting (HTS) magnetic WPs (Li *et al.*, 2014) in which the magnetic field regions are bounded by HTS films made of yttrium barium copper oxide (YBCO) deposited on sapphire (ceraco ceramic coating GmbH;[1] http://www.ceraco.de/hts-films/). The magnetic fields in neighboring regions thus change abruptly at the boundary between regions owing to the Meissner effect in the YBCO films. Previous experiments on the (Spin Echo Scattering Angle Measurement) SESAME (Parnell *et al.*, 2015) beamline at the pulsed Low Energy Neutron Source (Baxter *et al.*, 2005) (LENS) and the MAGIK (Dura *et al.*, 2006) instrument at the NIST Center for Neutron Research (NCNR) as well as simulations using the *MagNet*[1] (http://www.infolytica.com/) code have shown that the use of HTS films makes the fields within the WPs very homogeneous so we expect the intensity fringes produced for SEMSANS to have high contrast. All of the components through which neutrons pass cause very little attenuation or scattering of the neutron beam because they comprise thin (0.5 mm-thick) plates of single-crystal sapphire coated with 350 nm of YBCO and a thin (100 nm) gold layer. The magnetic fields within the device are generated using coils made of YBCO tape that are expected to be able to conduct at least 50 A at 77 K (Superpower Inc;[1] http://www.superpower-inc.com/), yielding fields up to 0.1 T at this temperature and higher fields at lower temperatures where the critical current is greater. These specifications are considerably beyond those currently available with room-temperature devices (Strobl, Tremsin *et al.*, 2012; Strobl, Weider *et al.*, 2012), even with water cooling (Pynn *et al.*, 2008; Stonaha *et al.*, 2013). The goal of our experiment was to investigate the use of these HTS WPs for SEMSANS since they hold the promise of extending the range of experiments to which this technique can be applied.

2. Spin echo modulated small-angle neutron scattering

The Larmor phase for neutrons propagating in a magnetic field is proportional both to the magnetic field integral along the neutron trajectory and to the neutron wavelength. A

[1] Certain commercial equipment, suppliers or software are identified in this paper to foster understanding. Such identification does not imply recommendation or endorsement by the National Institute of Standards and Technology, nor does it imply that the materials or equipment identified are necessarily the best available for the purpose.

single magnetic WP with uniform magnetic fields generates a Larmor phase (Φ_{WP}) along the neutron flight path that can be expressed as $\Phi_{WP} = c\,\lambda\,FI_{WP}$, where $c = 4.62 \times 10^{14}$ rad T^{-1} m^{-2} is a constant dependent on the neutron gyromagnetic ratio and mass, λ is the neutron wavelength, and FI_{WP} is the magnetic field integral along the neutron trajectory. In our case, assuming that the field is uniform in the WPs, this field integral can be expanded to leading order in the neutron beam divergence angle φ as

$$FI_{WP} = B(ay + by\varphi), \tag{2}$$

where B is the magnetic field intensity, and φ is the angle between the neutron path and the optic axis of the device, projected on the xy plane of Fig. 1(b). a and b are constants determined by the inclination angle of the hypotenuse (θ) shown in Fig. 1(b) and take the form of $a = 2\cot\theta$ and $b = 2(\cot\theta)^2$, where $\theta = 45^\circ$ in our case. In equation (2), the distance, y, is measured from the center of the WP. The term with coefficient a determines the accessible spin echo length for a given magnetic field, whereas the b term, in general nonzero, results from the symmetry of the device and is responsible for the lowest-order aberration. For the two WPs in the SEMSANS setup of Fig. 1(b), at distances of L_1 and L_2 from the detector plane, the total magnetic field integral for the neutrons incident at a particular point y on the detector can be written as follows:

$$FI^{T}_{WP} = a(B_1 - B_2)y + [a(B_1L_1 - B_2L_2) + b(B_1 - B_2)y]\varphi. \tag{3}$$

When equation (4) below is satisfied, the dependence of the field integral on the divergence angle, φ, is minimized since $y << L_1, L_2$ (Gähler, 2006):

$$B_1L_1 = B_2L_2. \tag{4}$$

The amplitude of the intensity modulation on the detector is proportional to the cosine of the Larmor phase since a polarization analyzer is placed in the beam. The period, p, of the intensity distribution on the detector is given by

$$p = \frac{2\pi}{c\lambda a(B_2 - B_1)}. \tag{5}$$

The spin echo length ξ, which is measured in the sample, depends on the distance from the sample to the detector plane through the equation

$$\xi = \lambda L_s/p. \tag{6}$$

Equation (6) gives the correct value of the spin echo length, independently of the ratio B_1/B_2, provided L_s is defined as the distance between the sample and the effective detector plane. If L_1 and L_2 are also both measured with respect to the effective detection plane, ξ is also equal to the separation of the neutron states at the sample, as shown in Fig. 1(b). Equation (6) implies that, for SEMSANS, the spin echo length can be calculated from the measured spatial period of the observed intensity fringes. This is different from the SESANS method, where the spin echo length has to be calculated from the magnetic fields within the WPs or calibrated in terms of scattering from a known structure such as a diffraction grating.

Without a sample, the intensity of the modulation on the detector can be written as $I_0 = T_0[V_0\cos(2\pi y/p) + 1]$, where T_0 depends on the incident neutron flux, V_0 is the Michelson visibility of the fringes, and the background is small and ignored. With a sample, the measured curve becomes $I_s = T_s[V_s\cos(2\pi y/p) + 1]$. Because of the scattering by the sample the visibility of the modulation is reduced so that

$$V_s/V_0 = \exp\{\Sigma_t[G(\xi) - 1]\}. \tag{7}$$

For a two-phase system with scattering length densities (SLDs) of ρ_p and ρ_s the quantity Σ_t is given by (Feigin & Svergun, 1987)

$$\Sigma_t = \lambda^2 t(\rho_p - \rho_s)^2\phi(1 - \phi)\zeta, \tag{8}$$

where t is the sample thickness, and ϕ and $(1 - \phi)$ denote the volume fractions of the two phases which, in the case of the experiment we report below, are suspended particles and solvent, respectively. ζ is the correlation length of the scattering system which, for a colloidal system, is related to the particle size and volume fraction of the sample (Andersson *et al.*, 2008; Washington *et al.*, 2014) and can be calculated exactly for a hard-sphere system with correlations described in the Percus–Yevick formalism (Percus & Yevick, 1958). Previous experiments with the colloid we used have demonstrated that correlations can be described by this formalism.

3. SEMSANS measurements

The SEMSANS measurements were performed on the MAGIK beamline (Dura *et al.*, 2006) at the NCNR using 5 Å ± 1% neutrons with a divergence of ±1.2° in the horizontal direction (**y**), using the setup shown in Fig. 2. Because the magnetic field inside the WPs is bounded by HTS films, the Larmor precession in between the two WPs can be started and stopped by simply putting guide fields (G_1 and G_4) with fields in the horizontal (**y**) direction outside each WP, within which the fields are along the **z** direction of Fig. 2. The effects of the spatial inhomogeneity in the guide fields G_2 and G_3 were minimized by introducing a current-sheet flipper (F) between them. Slits before the apparatus provided a 5 mm (**y**) × 5 mm (**z**) neutron beam to illuminate the sample. The neutron polarization analyzer used for this measurement was a single

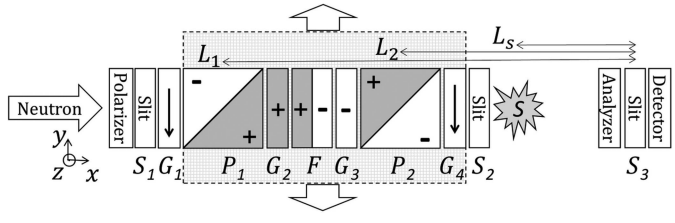

Figure 2
The SEMSANS experimental setup used on the reflectometer MAGIK at NCNR. The meshed box indicates the assembly that can be translated in the **y** direction.

supermirror in transmission mode and the neutron detector was a cylindrical ^{3}He detector, 25.4 mm in diameter. To obtain the high spatial resolution necessary to measure the intensity oscillation introduced by the two WPs, a fixed slit with a size of 0.5 mm in the **y** direction (S_3) was used at a distance of 26 cm in front of the detector, which is the furthest position from the sample because of the shielding block of the pencil detector. The distances L_1 and L_2 in Fig. 2 were 1.35 and 0.88 m, respectively, and the distance L_s was 0.70 m. In Fig. 2, B_1 and B_2 are the magnetic field intensities produced by WPs P_1 and P_2, respectively, and B_2 should be adjusted so that $B_2 = B_1L_1/L_2$. The values of B_1 and B_2 used in our experiment did not satisfy this relationship, causing a less than optimal visibility of the intensity modulation.

The fringes are measured by translating the two WPs and the electromagnetic guide fields between them in the **y** direction with respect to the fixed slit S_3, while keeping the neutron path between S_1 and the detector the same, as indicated by the meshed box in Fig. 2. The spin echo length is then scanned by increasing the current in the two WPs at a constant ratio of B_1/B_2. The sample measured was a colloidal silica suspension, which was prepared by mixing 0.5 g of SiO_2 particles (purchased from Fiber Optics), with an average radius of 90 nm, with 2.2 g of D_2O and 7.2 mg of ammonium hydroxide (Ashkar *et al.*, 2014). Samples were contained in 2 mm quartz cells (Hellma, USA). On the basis of the mass and the typical density of the silica powder (2.2 g cm^{-3}), the calculated volume fraction of silica in the sample is approximately 10%.

In terms of the SLD contrast between the particles and the solvent, which we write as $\rho_{\rm silica} - \rho_{\rm D_2O}$, the total cross section, Σ_t, can be calculated using equation (8), with a correlation length $\zeta \simeq 0.68 \times 2R$ (Andersson *et al.*, 2008). Here R is the particle radius, estimated using the Percus–Yevick formalism for hard particles at the volume fraction used. For our sample, Σ_t was approximately 0.4 at 5 Å.

In Fig. 3, two typical scans across the slit for the silica sample and a D_2O blank are shown at spin echo lengths of ξ = 87 nm and ξ = 210 nm. For $\xi < 210$ nm, such as in Fig. 3(*a*), each point on the curve took 25 s to measure and it took 16 h to measure both the silica sample and D_2O over a spin echo length range of 210 nm. The measurement time is long because, without a high-resolution position-sensitive neutron detector, we were obliged to translate the assembly across slit S_3 to obtain the required spatial resolution. We also wanted to measure several oscillation periods to check the uniformity of the intensity modulation produced by the WPs. Equivalent results for both the blank and the sample could be measured over the full range of spin echo lengths accessed in our experiment in ~30 min using a high-resolution detector (100 µm or less). To obtain good statistics at the longest spin echo length in the scan shown in Fig. 3(*b*) (ξ = 210 nm) and to determine Σ_t accurately from the asymptotic value of the measured signal at long spin echo lengths, each point was measured for 2 min. The intensity modulations for both the sample and the blank were fitted to a sinusoidal curve of the form $I = T_0[V_0 \cos(2\pi y/p + \delta) + 1]$, where δ is the offset of the fringes from the centre of the WP. For both spin echo lengths shown in Figs. 3(*a*) and 3(*b*), it is clear that the amplitude of the oscillation is reduced by the scattering from the sample.

The amplitude of the oscillation and the mean value of the intensity can be extracted for both D_2O and the sample for each scan. In fact, we could have used an empty beam instead of a D_2O blank for the purposes of calculating the sample correlation function. However, using the D_2O blank allows us to see directly the total attenuation of the beam due the colloidal particles: this shows up as the difference between the average values of the intensity for the two curves in each panel of Fig. 3. To quantify the performance of the setup we plot the visibility of the intensity modulation, measured with the D_2O blank, as a function of spin echo length. As Fig. 4 shows, the visibility without a scattering sample decreases from 80% at short spin echo length to 60% at the longest spin echo length (210 nm). This decrease is due primarily to the use of the

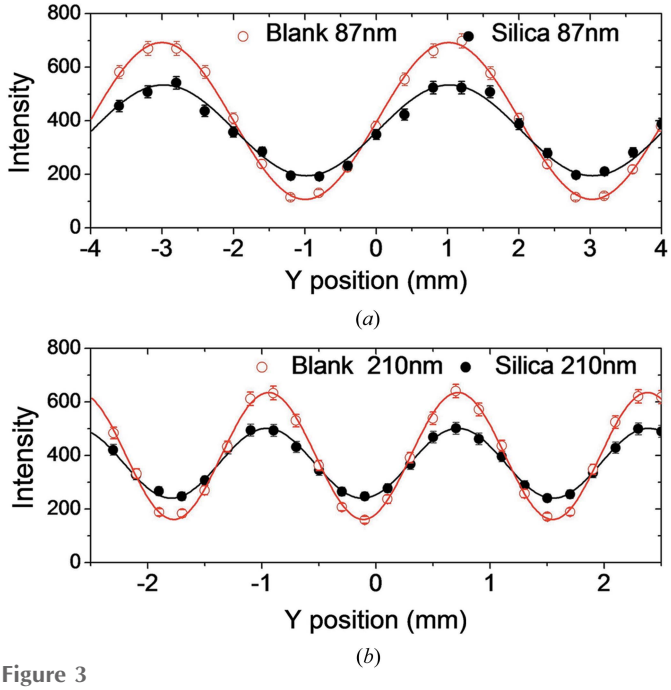

Figure 3
Two typical scans for the silica sample and D_2O at different spin echo lengths of (*a*) 87 nm and (*b*) 210 nm. Error bars indicate ±1 standard deviation in all the plots shown in this paper.

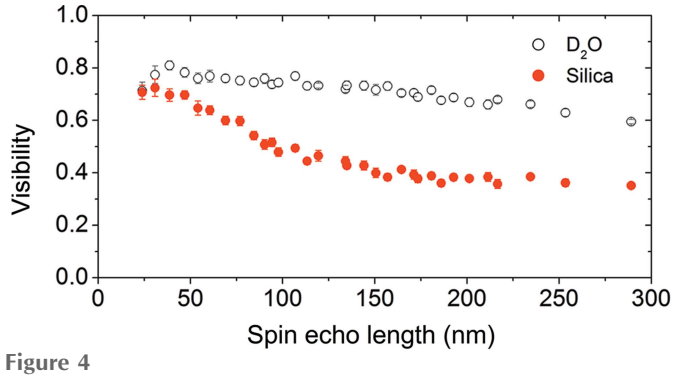

Figure 4
Modulation visibility for D_2O and silica at various spin echo lengths.

0.5 mm slit S_3. As the spin echo length increases, the period of the oscillation, p, decreases, thereby reducing the measured fringe contrast owing to the averaging over the width of the slit. At short spin echo length, where the spatial period is ~20 mm, the intensity averaging due to the slit is negligible. As we show below, the loss of contrast at small spin echo lengths (*i.e.* from 100 to 80%) is mainly due to a slight offset in the **z** direction between the electromagnetic guides G_2 and G_3 in Fig. 2.

The ratio of the two curves in Fig. 4 is shown in Fig. 5. This quantity is the same as P/P_0 measured in a SESANS experiment, as indicated in equations (1) and (7).

A sample of the same silica particles was measured using the instrument Offspec at ISIS in SESANS mode (Dalgliesh *et al.*, 2011). This measurement showed that 68% of the actual particle is composed of silica, while the rest consists of solvent that has penetrated into the particle. To confirm this, SANS measurements were also performed on a colloidal suspension in D_2O with a well defined small volume fraction (0.2654×10^{-3}). Fits of the SANS data to a sphere model, with the colloidal particle SLD, ρ_p, being the only fit parameter, yield $\rho_p = 4.335 \times 10^{-4}$ nm^{-2}. Knowing the SLD of D_2O, $\rho_{D_2O} = 6.0 \times 10^{-4}$ nm^{-2}, and the SLD of silica, $\rho_{silica} = 3.5 \times 10^{-4}$ nm^{-2} (obtained from SANS contrast variation measurements), we find that 66.6% of the actual particle is silica, which is very close to the SESANS results. These values were used to compute the total scattering from equation (8).

The correlation function $G(\xi)$ of the colloidal silica sample can be calculated using the Percus–Yevick hard-sphere model (Percus & Yevick, 1958). The resulting intensity ratio for the SEMSANS experiment, obtained using equation (7), is shown in Fig. 5. The good agreement between the SEMSANS experimental results and calculations corroborates the sample parameters obtained by the SANS and SESANS measurements and indicates that the SEMSANS setup operates in the manner expected.

4. Discussion of the SEMSANS measurements

The amplitude of the intensity modulation measured in our experiment at short spin echo lengths is significantly lower than we expected, based on the measurements of the spin transport efficiency of an individual WP (Li *et al.*, 2014). To investigate possible causes for this effect we carried out simulations using the Monte Carlo package *McStas* (Willendrup *et al.*, 2004; Lefmann & Nielsen, 1999) set up to mimic both the divergence and wavelength distribution of the neutron beam used in our experiment. Using *McStas*, Sales *et al.* (2015) have also studied the importance of tuning the setup to keep the signal in the spin echo condition to avoid asymmetries of the fringes.

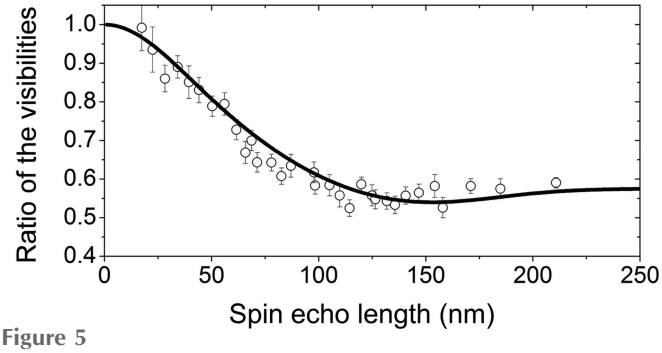

Figure 5
The ratio of the visibility of the fringes of silica colloid and blank described in the text, measured (points) and calculated (line) as a function of spin echo length.

The two electromagnetic field guides (G_1 and G_2 in Fig. 2) used for this experiment consist of pairs of pancake coils with soft iron cores and a Mu-metal yoke for magnetic flux return. Owing to the use of soft iron, the magnetic field between the pole pieces depends strongly on the distance from the pole pieces. Thus, the magnetic field integral along the neutron trajectory is inhomogeneous across the neutron beam and depends on the distance between the neutron trajectory and the centre of the device. A small error in placing one of these guide fields may therefore result in incomplete cancellation of Larmor phases on opposite sides of the current sheet flipper, at least for some neutron paths. To characterize the performance of these two electromagnets in our experiment, the magnetic field distribution due to the electromagnets and the current sheet flipper was simulated using the commercially available finite-element software *MagNet*. Because of the geometrical symmetry of our SEMSANS setup, the magnetic field integral between each WP and the current sheet can be expanded as a function of the divergence angles φ and ψ in the xy and xz planes, respectively, as

$$\mathrm{FI}_{\mathrm{EM}}(y, z, \varphi, \psi) = \text{const.} + a_{\mathrm{EM}} y^2 + b_{\mathrm{EM}} z^2 + c_{\mathrm{EM}} y\psi + d_{\mathrm{EM}} z\psi, \tag{9}$$

where y and z are the position of the neutron as it passes through the central current sheet, measured with respect to the optic axis of the device. The coefficients in this equation are obtained from the *MagNet* simulations as const. = 92.4 mT cm, $a_{\mathrm{EM}} = -0.175$ mT mm^{-1}, $b_{\mathrm{EM}} = 0.626$ mT mm^{-1}, $c_{\mathrm{EM}} = 41.35$ mT rad^{-1} and $d_{\mathrm{EM}} = -134.7$ mT rad^{-1}. The spatial variations of the orientation and magnitude of the guide fields are small enough to allow the neutron spin to follow the guide fields without significant depolarization, as we have verified using an iterative solution of the Bloch equation (Seeger & Daemen, 2001). In this situation, equation (9) can be used to calculate the Larmor phase generated by the electromagnets and the current sheet for any neutron trajectory. We include in our model a possible offset of $\pm\Delta y/2$ and $\pm\Delta z/2$ away from the beam centre for the two WPs. The total field integral for a particular beam trajectory can then be written as

$$\begin{aligned}\mathrm{FI}^{\mathrm{T}}_{\mathrm{EM}} &= \mathrm{FI}^{1}_{\mathrm{EM}}(y + \Delta y/2, z + \Delta z/2, \varphi, \psi) \\ &\quad - \mathrm{FI}^{2}_{\mathrm{EM}}(y - \Delta y/2, z - \Delta z/2, -\varphi, -\psi) \\ &= (2a\Delta y + 2c\varphi)y + (2b\Delta z + 2d\psi)z + O(y^2, z^2, \varphi^2, \psi^2).\end{aligned} \tag{10}$$

It is evident that the total magnetic field integral and hence the Larmor phase between the two WPs is y and z dependent if the two electromagnetic guide fields are offset relative to each

other, because such an offset generates a field integral gradient along both the **y** and **z** direction. Given a field integral gradient, a spatial oscillation of neutron intensity will be obtained in the direction parallel to the gradient. For the WPs alone, the field integral gradient is along the **y** direction, and thus the y component of $\nabla \mathrm{FI}_{\mathrm{EM}}^{\mathrm{T}}$ can either increase or decrease the spatial period of the oscillation introduced by the WPs. This will not affect the calibration of the spin echo length, since this quantity is determined using the actual spatial period of the observed intensity fringes. However, a nonzero z component of $\nabla \mathrm{FI}_{\mathrm{EM}}^{\mathrm{T}}$ will deviate the field integral gradient from the **y** direction, so that the intensity fringes will no longer be parallel to the **z** direction.

The *McStas* simulation was carried out with the monochromator on the MAGIK beamline replaced by a neutron source whose size is more than large enough to fill the divergence transmitted by slits S_1 and S_3 in Fig. 2 (S_2 does not limit the divergence and simply suppresses background). The wavelength distribution was chosen to mimic the monochromator used on MAGIK. Instead of using a pencil detector and S_3, a 20 × 20 mm position-sensitive detector with 512 × 512 pixels was used in the simulation, allowing the full y and z dependence of the neutron intensity to be recorded at the position of S_3 with high resolution. Clearly the position of the actual detector used in the experiment is irrelevant since, provided it is large enough, it will register the same count rate whatever its distance behind the slit S_3. Fig. 6 shows the simulated counts for a field of 16 mT in P_1 and 22.5 mT in P_2. For Fig. 6(*a*), the two electromagnets are aligned with the beam centre in both the **y** and **z** directions, while for Fig. 6(*b*), there is an offset of 2 mm between them in the **z** direction.

Fig. 6(*a*) shows that if the two guide field electromagnets are aligned the spatial fringes are parallel to the **z** direction and the corresponding fringe visibility is close to unity. This means that the magnetic field integral inhomogeneity caused by G_2 and G_3 can be compensated by the magnetic field reversal introduced by the current sheet. However, Fig. 6(*b*) shows that, by introducing an offset of 2 mm between these two electromagnets in the **z** direction, the fringes can be tilted with the tilting angle defined by the ratio between the **z** and **y** components of the magnetic field integral gradient of the whole setup. Because the fringes tilt in this case, measurement of them using a narrow slit aligned along **z** will tend to average the intensity over a substantial part of one period, causing a

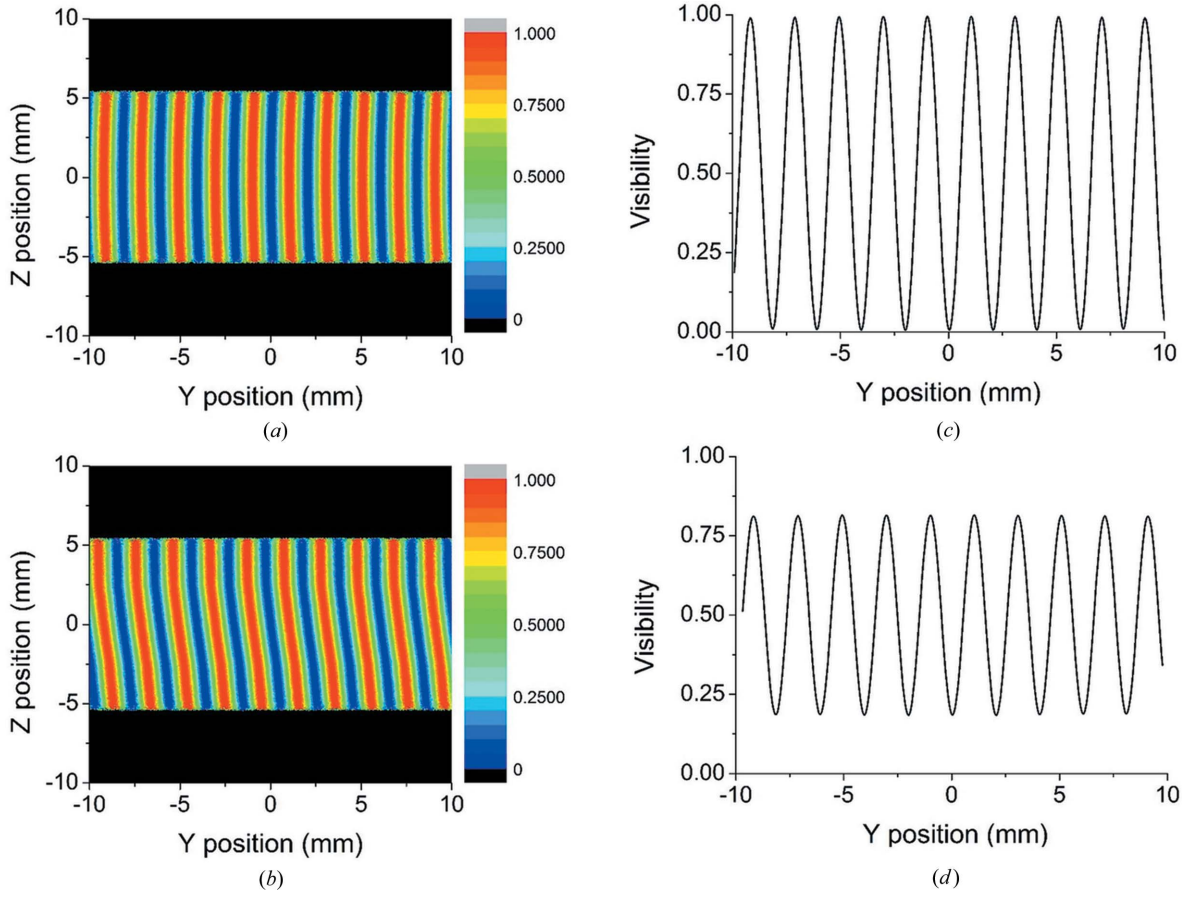

Figure 6
(*a*), (*b*) False color plot of the spatial variation of the neutron intensity at the position of S_3 in Fig. 2, simulated by *McStas*. (*c*), (*d*) The corresponding intensity integrated along the **z** direction over a 0.5 mm-wide slit in the **y** direction to simulate the pencil detector and the narrow slit, S_3, used in our experiment. For both simulations, the magnetic field in P_2 is 22.5 mT. (*a*), (*c*) The intensity when the electromagnets G_2 and G_3 are aligned. (*b*), (*d*) The intensity when the two electromagnets are offset by 2 mm from each other in the **z** direction. The color scales indicate the neutron intensity normalized to the maximum intensity on the detector.

decrease in the visibility of the fringes, as shown in Fig. 6(*d*). For different spin echo lengths, the fringes are always tilted by the same fraction of the corresponding period; hence the depolarization due to the offset between the two electromagnets is a constant for various spin echo lengths.

Fig. 7 shows the fringe visibility V_0 for various offsets between the two electromagnets, with the spatial fringes integrated along the **z** direction. It is clear that the fringe visibility is very sensitive to the offset between guide fields. Since the two electromagnets were not aligned in the experiments with a precision better than 1–2 mm, we believe that this effect explains the observed low fringe visibility that is inconsistent with the known high spin-transport efficiency of the WPs themselves (Li *et al.*, 2014).

In our experiment, the ratio between B_1 and B_2 was obtained from the position of a pencil detector instead of the slit S_3, which means the requirement of $B_1L_1 = B_2L_2$ for maximum possible fringe visibility is not properly satisfied at the slit position. This effect is included in the *McStas* simulations described above. To evaluate the magnitude of the effect for the fringes with the same period, a second *McStas* simulation was performed with B_1 = 12 mT and B_2 = 18.5 mT, such that the ratio between the fields is correct for a detector placed at the position of S_3. The results for the two different field settings for the slit widths used in our experiment (in particular, for S_1 = 5 mm) are compared in Fig. 8, which shows a ∼15% difference in the fringe visibility for the different settings of B_1 and B_2. When S_1 is opened up to 10 mm, however, the ratio of B_1 to B_2 has a larger effect and fringe visibility can be preserved only by tuning them correctly. This is exactly what we would expect since the ideal ratio of B_1 and B_2 is chosen so that the visibility of the intensity modulation at the detector is unaffected by beam divergence.

Overall, our *McStas* simulations allow us to account for all of the results we obtained and also point to the robustness of the SEMSANS technique in suboptimal configurations. The technique depends only on achieving a set of equal-amplitude intensity oscillations at the detector position. If the visibility of the oscillations is less than optimal, the statistical accuracy of the measured correlation function will be reduced but measurement is still possible.

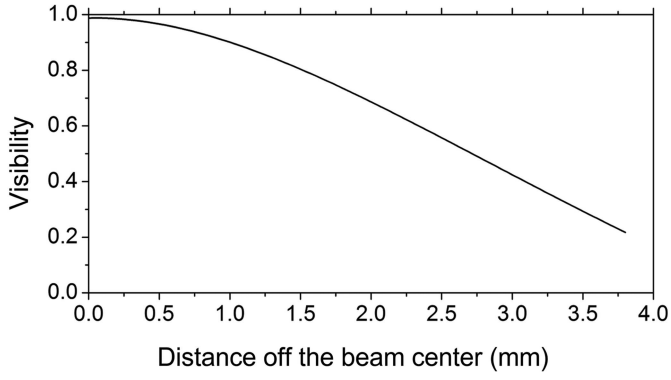

Figure 7
The visibility of the intensity modulations simulated by *McStas* as a function of the offset between the two electromagnets in the **z** direction.

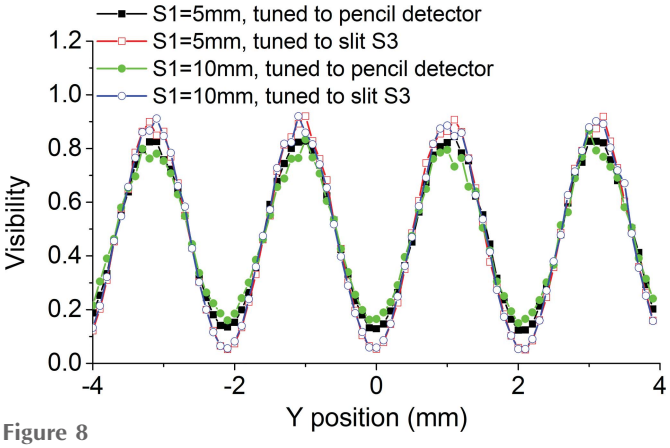

Figure 8
Monte Carlo simulations of the effect of the different B_1 and B_2 settings for different size of S_1. The two electromagnets are properly aligned and the simulation uses the same setup as the actual experiment, including the slits and pencil detector.

5. Conclusion

Using two HTS Wollaston prisms, we have measured the correlation function $G(\xi)$ for a colloidal silica sample by SEMSANS and obtained a result that exactly reproduces the result obtained with an identically prepared sample using SESANS. We have simulated our experiment using the *McStas* code and shown that the lower than expected fringe visibility is most likely due to inadequate alignment of guide fields between the two WPs, coupled with the use of a narrow slit to obtain sufficient spatial resolution for accurate intensity measurements. The results of the *McStas* simulation show that the SEMSANS method is robust even when not set up in an optimal manner. In this experiment, we did not attempt to increase the current in our WPs to the maximum value because the resulting modulation period would have become too small for us to measure accurately. The magnetic field in P_2 was 30 mT for the experiments reported here, and it has been tested up to 50 mT. Our most recent generation of Wollaston prisms has been tested up to 70 mT and is designed to produce 170 mT. If that prism had been used in our present setup at its design limit we would, given an adequate detector, have measured a maximum spin echo length of about 1.2 µm using neutrons with a wavelength of 5 Å. A further increase in spin echo length could easily be achieved by increasing the distance between the sample and the effective detector plane beyond the value (0.7 m) used in this experiment, which was limited by geometrical constraints of the instrument used.

Acknowledgements

The conceptual design and simulations of the first HTS Wollaston prism were supported by the National Science Foundation (grant No. DMR-0956741). The design and construction of the two magnetic Wollaston prisms were

supported by the STTR program of the US Department of Energy (grant No. DE-SC0009584). We would like to extend our gratitude to Dr J. Plomp (Delft University of Technology) for providing the current-sheet flipper, J. Doskow (Indiana University Bloomington) for designing the vacuum chamber, and the members of the sample environment team at the NCNR, Tanya Dax and Qiang (Alan) Ye, for their help with the cryogenics. We also acknowledge the support of the National Institute of Standards and Technology, US Department of Commerce, in providing access to the neutron research facilities, supported in part by the National Science Foundation under grant No. DMR-0944772. Construction of LENS was supported by the National Science Foundation grants DMR-0220560 and DMR-0320627, the 21st Century Science and Technology fund of Indiana, Indiana University, and the Department of Defense.

References

Andersson, R., van Heijkamp, L. F., de Schepper, I. M. & Bouwman, W. G. (2008). *J. Appl. Cryst.* **41**, 868–885.
Ashkar, R., Pynn, R., Dalgliesh, R., Lavrik, N. V. & Kravchenko, I. I. (2014). *J. Appl. Cryst.* **47**, 1367–1373.
Baxter, D. V., Cameron, J. M., Derenchuk, V. P., Lavelle, C. M., Leuschner, M. B., Lone, M. A., Meyer, H. O., Rinckel, T. & Snow, W. M. (2005). *Nucl. Instrum. Methods Phys. Res. Sect. B*, **241**, 209–212.
Bonse, U. & Hart, M. (1965). *Appl. Phys. Lett.* **7**, 238–240.
Bouwman, W. G., Duif, C. P., Plomp, J., Wiedenmann, A. & Gähler, R. (2011). *Phys. B Condens. Matter*, **406**, 2357–2360.
Bouwman, W. G., Kraan, W. & Rekveldt, M. T. (1999). *Phys. B Condens. Matter*, **267–268**, 79–83.
Bouwman, W. G., van Oossanen, M., Uca, O., Kraan, W. H. & Rekveldt, M. T. (2000). *J. Appl. Cryst.* **33**, 767–770.
Brezger, B., Hackermüller, L., Uttenthaler, S., Petschinka, J., Arndt, M. & Zeilinger, A. (2002). *Phys. Rev. Lett.* **88**, 100404.
Dalgliesh, R. M., Langridge, S., Plomp, J., de Haan, V. O. & van Well, A. A. (2011). *Phys. B Condens. Matter*, **406**, 2346–2349.
Dura, J. A., Pierce, D. J., Majkrzak, C. F., Maliszewskyj, N. C., McGillivray, D. J., Lösche, M., O'Donovan, K. V., Mihailescu, M., Perez-Salas, U., Worcester, D. L. & White, S. H. (2006). *Rev. Sci. Instrum.* **77**, 074301.
Feigin, L. A. & Svergun, D. I. (1987). *Structure Analysis by Small-Angle X-ray and Neutron Scattering.* New York: Plenum Press.
Gähler, R. (2006). Presented at PNCMI Polarized Neutron School, 25–28 September 2006, Berlin, Germany.
Gähler, R., Golub, R. & Keller, T. (1992). *Phys. B Condens. Matter*, **180–181**, 899–902.
Golub, R. & Gähler, R. (1987). *Phys. Lett. A*, **123**, 43–48.
Krouglov, T., de Schepper, I. M., Bouwman, W. G. & Rekveldt, M. T. (2003). *J. Appl. Cryst.* **36**, 117–124.
Lefmann, K. & Nielsen, K. (1999). *Neutron News*, **10**(3), 20–23.
Li, F., Parnell, S. R., Hamilton, W. A., Maranville, B. B., Wang, T., Semerad, R., Baxter, D. V., Cremer, J. T. & Pynn, R. (2014). *Rev. Sci. Instrum.* **85**, 053303.
Major, J., Vorobiev, A., Rühm, A., Maier, R., Major, M., Mezger, M., Nülle, M., Dosch, H., Felcher, G. P., Falus, P., Keller, T. & Pynn, R. (2009). *Rev. Sci. Instrum.* **80**, 123903.
Parnell, S. R., Washington, A. L., Li, K., Yan, H., Stonaha, P., Li, F., Wang, T., Walsh, A., Chen, W. C., Parnell, A. J., Fairclough, J. P. A., Baxter, D. V., Snow, W. M. & Pynn, R. (2015). *Rev. Sci. Instrum.* **86**, 023902.
Percus, J. & Yevick, G. (1958). *Phys. Rev.* **110**, 1–13.
Pfeiffer, F., Grünzweig, C., Bunk, O., Frei, G., Lehmann, E. & David, C. (2006). *Phys. Rev. Lett.* **96**, 215505.
Pynn, R., Fitzsimmons, M. R., Lee, W. T., Stonaha, P., Shah, V. R., Washington, A. L., Kirby, B. J., Majkrzak, C. F. & Maranville, B. B. (2009). *Phys. B Condens. Matter*, **404**, 2582–2584.
Pynn, R., Lee, W. T., Stonaha, P., Shah, V. R., Washington, A. L., Kirby, B. J., Majkrzak, C. F. & Maranville, B. B. (2008). *Rev. Sci. Instrum.* **79**, 063901.
Rekveldt, M. T. (1996). *Nucl. Instrum. Methods Phys. Res. Sect. B*, **114**, 366–370.
Rekveldt, M. T., Bouwman, W. G., Kraan, W. H., Uca, O., Grigoriev, S. V., Habicht, K. & Keller, T. (2002). *Neutron Spin Echo Spectroscopy*, Lecture Notes in Physics Vol. 601, edited by F. Mezei, C. Pappas & T. Gutberlet, pp. 87–99. Berlin, Heidelberg: Springer-Verlag.
Sales, M., Plomp, J., Habicht, K. & Strobl, M. (2015). *J. Appl. Cryst.* **48**, 92–96.
Schaefer, D. W. & Agamalian, M. M. (2004). *Curr. Opin. Solid State Mater. Sci.* **8**, 39–47.
Seeger, P. A. & Daemen, L. L. (2001). *Nucl. Instrum. Methods Phys. Res. Sect. A*, **457**, 338–346.
Stonaha, P., Hendrie, J., Lee, W. T. & Pynn, R. (2013). *Rev. Sci. Instrum.* **84**, 105113.
Strobl, M. (2014). *Sci. Rep.* **4**, 7243.
Strobl, M., Tremsin, A. S., Hilger, A., Wieder, F., Kardjilov, N., Manke, I., Bouwman, W. G. & Plomp, J. (2012). *J. Appl. Phys.* **112**, 014503.
Strobl, M., Wieder, F., Duif, C. P., Hilger, A., Kardjilov, N., Manke, I. & Bouwman, W. G. (2012). *Phys. B Condens. Matter*, **407**, 4132–4135.
Washington, A. L., Li, X., Schofield, A. B., Hong, K., Fitzsimmons, M. R., Dalgliesh, R. & Pynn, R. (2014). *Soft Matter*, **10**, 3016–3026.
Willendrup, P., Farhi, E. & Lefmann, K. (2004). *Phys. B Condens. Matter*, **350**, E735–E737.